Solution-processed $CaMnO_{3-\delta}$-based all oxide solar cells with high open-circuit voltage

Parul Garg,[1] Sanchari Bhattacharya,[2] Sakal Singla,[1] Priya Kaith,[1] Sanjoy Datta,[2] Biswanath Chakraborty,[1] and Ashok Bera[1,*]

[1]*Department of Physics, Indian Institute of Technology Jammu, Jammu and Kashmir 181221, India*
[2]*Department of Physics and Astronomy, National Institute of Technology Rourkela, Odisha 769008, India*

(Received 27 May 2022; revised 8 July 2022; accepted 19 July 2022; published 9 August 2022)

Finding a low-cost, stable solar absorber with suitable optical properties is one of the key aspects in promoting solar cell research. Perovskite-structured $CaMnO_3$, composed of earth-abundant elements, is an environmentally friendly multifunctional material especially featuring thermoelectricity and G-type antiferromagnetism. In this paper, we explore the potential of $CaMnO_{3-\delta}$(CMO) as an absorber layer in all oxide solar cells. Solution-processed CMO shows strong light absorption capacity in the wavelength range of 400–750 nm with the estimated optical bandgap of 1.77 eV. First-principles calculations show *d*-*d* transitions within the upper Mott-Hubbard bands, and lower Mott-Hubbard bands constitute the electronic bandgap, whereas the *p*-*d* transitions between the O 2*p* and Mn 3*d* bands contribute to the optical absorption in the visible region. Furthermore, a gradual increase in the current value was observed under illumination in the photoconductivity measurement. We have designed a CMO absorber-layer-based all oxide solar cell using a conventional mesostructured TiO_2 photo-anode and NiO hole transport layer (HTL). The suitable band alignment of the CMO absorber with both TiO_2 and NiO enables us to achieve an average open-circuit voltage (V_{OC}) of 0.92 V with the maximum value of 1.03 V, which is among the highest reported values so far for oxide-based solar cells. Solar cell parameters were also validated using simulations. Our results add a direction in the search for low-cost, stable solar absorber materials.

DOI: 10.1103/PhysRevMaterials.6.085402

I. INTRODUCTION

Perovskite-structured manganites with the chemical formula $RMnO_3$, where R is a trivalent rare-earth cation or divalent alkaline-earth cation (R = La, Ba, Nd, Ca, Sr, Y, Pr, etc.), exhibit unique electric and magnetic properties [1–3] and have been extensively used in many practical applications like magnetoresistance switching [4], fuel cells [5], and gas sensing [6], to name a few. Ca and Mn are present at the 5th and 12th positions [7,8] in the most earth-abundant metal list, making $CaMnO_3$ one of the cheapest materials among the existing sustainable manganites. The high negative Seebeck coefficient ($S \sim -350\,\mu V\,K^{-1}$) makes it a promising thermoelectric material [9]. Recently, $CaMnO_3$ has been used in energy storage [10,11], as an electrocatalyst [12], and as a buffer layer in solar cells [13], confirming its multifunctionality.

In general, oxides are environmentally stable and extensively used as electron transport layer (ETL) or hole transport layer (HTL) in solar cells [14–19]. Some oxides have also been used as active absorber layers [20,21]. Complex oxides possess bandgap tunability with the change in chemical compositions providing an auxiliary advantage in designing multijunction solar cells or panchromatic solar cells [22–24]. Hence, some perovskite oxides like $BaTiO_3$ [25], $BiFeO_3$ [26,27], $LaVO_3$ [28], $KNbO_3$ [29,30], and $Pb(Zr, Ti)O_3$ [31] have been used as active absorber layers in solar cells. Among them, $BaTiO_3$, $BiFeO_3$ and $Pb(Zr, Ti)O_3$ have large bandgaps, restricting their light absorption capacity to a shorter wavelength range in the solar spectrum, while La and V being expensive, do not provide cost-effective solutions. Environmentally friendly *n*-type semiconducting $CaMnO_3$ has an experimental direct bandgap of 1.55 [32] to 1.75 eV [33] with high absorption coefficient of $10^5\,cm^{-1}$ and a fast charge carrier mobility of 0.02–0.05 $cm^2\,V^{-1}\,s^{-1}$ [34], making it a promising absorber material in solar cells.

In this paper, we have synthesized $CaMnO_{3-\delta}$ (CMO) thin films using the sol-gel spin coating technique and studied their optical and optoelectronic properties. The solution-grown CMO thin film shows a direct optical bandgap of 1.77 eV with an absorption coefficient $> 10^4\,cm^{-1}$. Density functional theory (DFT) has also been employed to explain the electronic band structure and the origin of light absorption in the visible spectrum. Furthermore, on broadband light illumination, CMO film shows about a 2.5-fold increase in the current value over the dark current. Based on the suitable optical and photoconducting nature of CMO, we have fabricated an all oxide solar cell using CMO as an absorber. In a conventional sensitized solar cell architecture, with mesoporous TiO_2 (m-TiO_2) as an electron transporting layer and NiO as a solid-state HTL, we could achieve a maximum open-circuit voltage (V_{OC}) of 1.03 V with an average of 0.92 V, which is among the highest reported V_{OC} for all oxide-based solar cells. To validate our results, we have also simulated our device performance using SCAPS software. The increase in the V_{OC} after adding a NiO HTL mainly originated due to the suitable band alignment of

*ashok.bera@iitjammu.ac.in

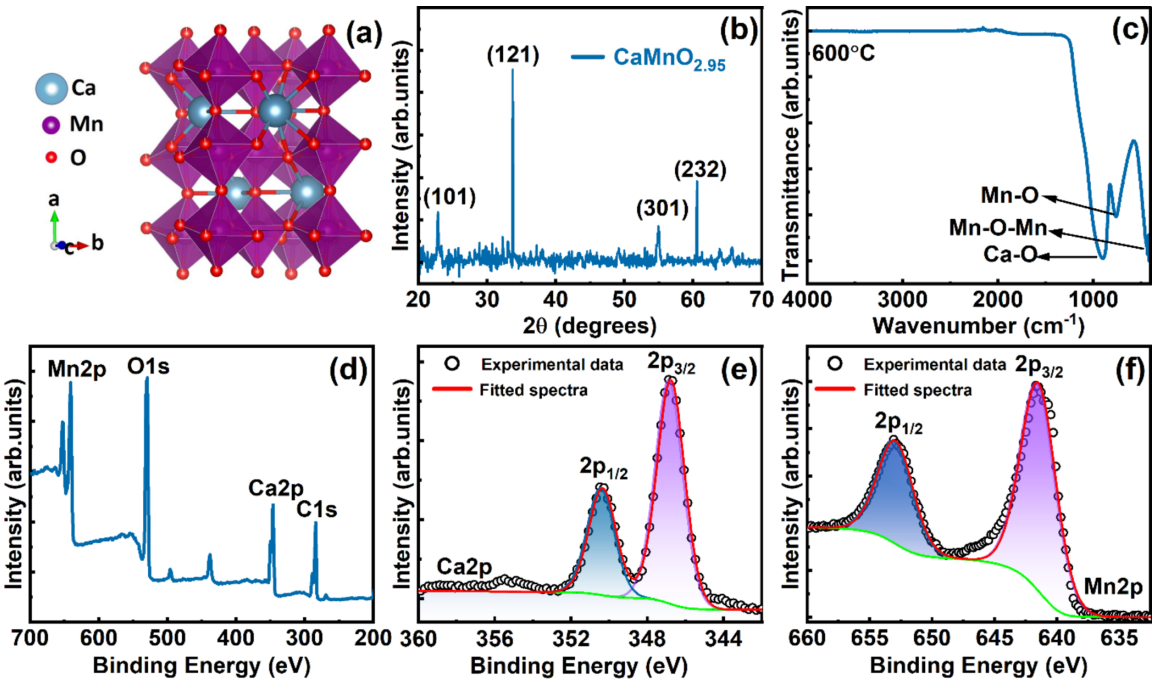

FIG. 1. (a) Schematic of the orthorhombic crystal structure of CMO. (b) X-ray diffraction (XRD) pattern of CMO thin film. (c) Fourier transform infrared (FT-IR) spectra of CMO film. (d) X-ray photoelectron spectroscopy (XPS) survey scan spectra of CMO thin film. High-resolution XPS spectra of (e) Ca 2*p* and (f) Mn 2*p*.

CMO with the charge transporting layers. Our results provide a substructure for further research in cost-effective and environmentally friendly stable oxide photo-absorber materials for all oxide solar cells or the high bandgap top subcell in monolithic tandem solar cells.

II. EXPERIMENTAL SECTION

CMO thin film was deposited on a glass substrate using the solution-processed spin coating method. In brief, 0.25 M precursor solution of CMO was made by adding stoichiometric amounts of calcium nitrate tetrahydrate [$Ca(NO_3)_2 4H_2O$] and manganese nitrate hydrate [$Mn(NO_3)_2 H_2O$] in glacial acetic acid at room temperature. A small amount of ethanol and methanol were added to prepare a homogeneous and transparent solution. All chemicals were $> 99.9\%$ pure and purchased from Sigma-Aldrich. The solution was stirred at 70 °C continuously for 3 h. To maintain the pH value of the solution at 4.1, a small amount of triethanolamine was added. The films were then deposited on the glass substrate by spin coating at 2000 rpm for 60 s. The films were first dried at 350 °C for 10 min to remove the organic solvents, then finally annealed at 600 °C for 2 h for crystallization [35]. A similar process was repeated to deposit multiple layers of the films to get the desired film thickness. The x-ray diffraction (XRD) pattern was characterized using Cu Kα radiation, $\lambda = 1.5406$ Å (Panalytical Empyrean), and the data were analyzed using X'Pert High Score software. The surface morphology of the films was studied by field emission scanning electron microscope (FESEM; JEOL JSM 7900F). The Fourier transform infrared (FT-IR) spectrum was obtained by Nicolet IS50-Thermo scientific instrument from 4000 to 400 cm^{-1}. Chemical composition and the oxidation states of Ca and Mn ions in CMO thin films were estimated by x-ray photoelectron spectroscopy (XPS; Nexsa-ThermoFisher). The binding energies obtained in the XPS spectra were corrected concerning the C1s peak at 284.8 eV. The absorption spectrum of the CMO film was acquired by a UV-Vis-NIR spectrophotometer (Cary 5000). To measure the photoluminescence (PL) spectrum, the CMO film was excited by a He-Cd laser (wavelength 325 nm, Kimmon Koha Co. Ltd.; model KR1801C), and the emission spectrum was recorded using a high-resolution spectrometer (Horiba Jobin Yvon model iHR 320). Ultraviolet photoelectron spectroscopy (UPS) measurements were performed using He (I) ($E_{max} - 21.22$ eV) source (Nexsa-ThermoFisher) to estimate the ionization energy of CMO.

The solar cells were fabricated on FTO-coated glass substrates using spin coating following our previous report [16]. In brief, compact TiO_2 (c-TiO_2) was deposited from the acidic solution of titanium isopropoxide followed by annealing at 500 °C. Then m-TiO_2 was deposited on top of the c-TiO_2 layer from a diluted titania paste (dyesol 18NR-T) and then annealed at 550 °C for 1 h. A layer of CMO precursor solution of $\sim$30 μL is then deposited to add the absorber layer followed by a layer of NiO HTL from the nickel acetate solution. Finally, the top contact was made by depositing a 100 nm Ag electrode using thermal evaporation, and the final device area was 0.01 cm^2.

III. RESULTS AND DISCUSSION

Perovskite-structured CMO shows antiferromagnetic behavior at room temperature and crystallizes into a *Pnma* structure [13] in which Mn cations are present at the center of the octahedron, while Ca cations exist at the 12 coordinate positions, as shown in Fig. 1(a). The XRD pattern of the thin film

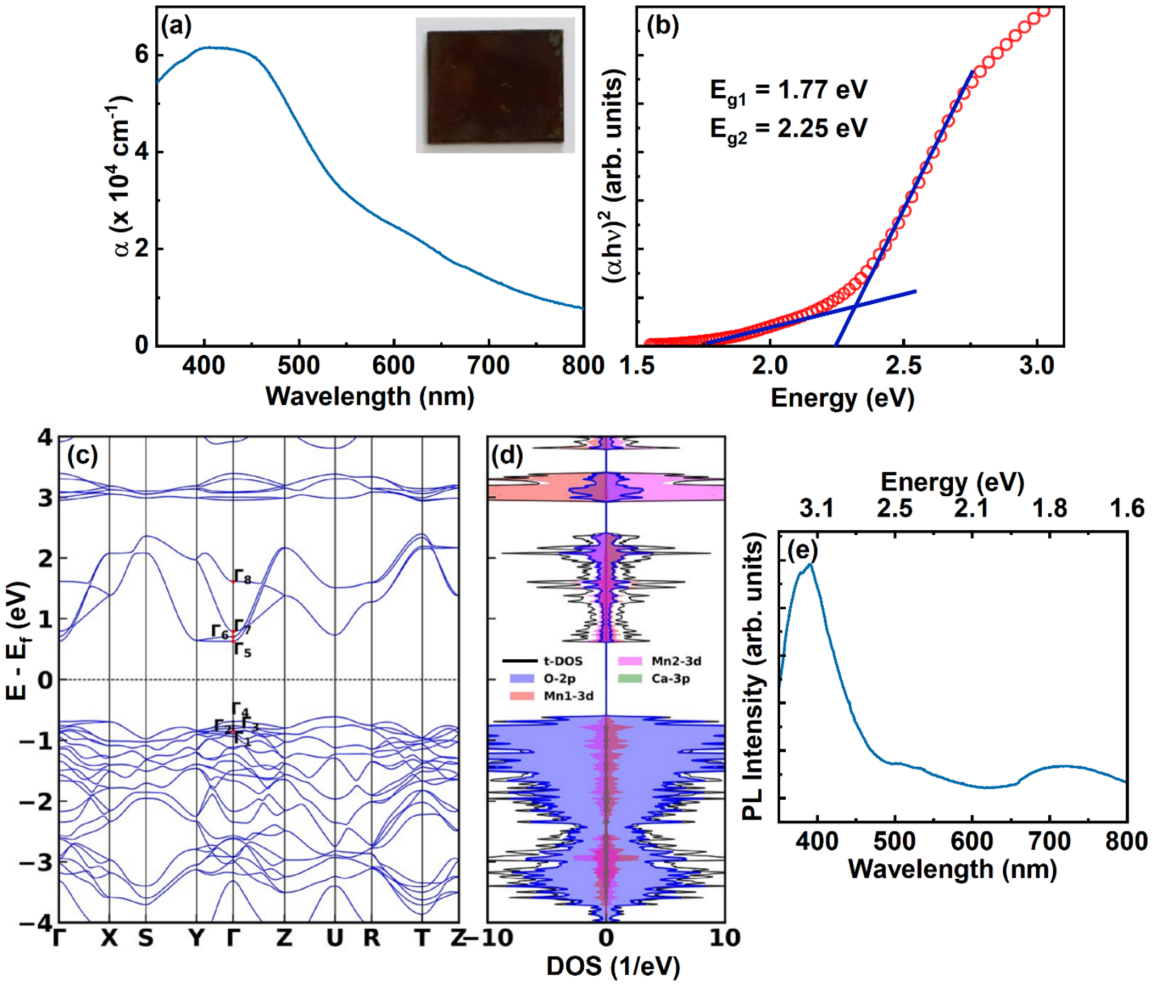

FIG. 2. (a) Optical absorption spectra of the CMO thin film, and the inset shows an optical image of CMO film. (b) Tauc plot of CMO thin film. (c) Electronic band structure of CMO and (d) density of states (DOS) with partial contributions from O 2p, Mn1 3d, Mn2 3d, and Ca 3p. (e) Photoluminescence (PL) spectra of CMO thin film.

deposited on a glass substrate shown in Fig. 1(b) matched with $CaMnO_{3-\delta}$ where $\delta = 0.05$ as obtained from the crystallographic open database (COD) reference number 96-152-5995, and estimated lattice parameters are $a = 5.28$ Å, $b = 7.46$ Å, and $c = 5.27$ Å, showing the phase formation of $CaMnO_{2.95}$. The FT-IR spectrum of the CMO thin film in Fig. 1(c) shows a band at ∼410 cm^{-1} due to the changes in the bond angle of the bending mode of Mn-O-Mn; the peak at 760 cm^{-1} is most likely characteristic of Mn-O lattice vibration, and a strong absorption band at ∼890 cm^{-1} corresponds to the Ca-O bonds [36,37]. No other bands are present at the higher wave numbers, confirming the absence of any other phases. The XPS survey scan spectra of the CMO film in Fig. 1(d) shows only the presence of calcium, manganese, and oxygen, indicating the purity of the CMO sample. The high-resolution XPS spectra of the Ca 2p in Fig. 1(e) show two distinct peaks of Ca $2p_{1/2}$ and Ca $2p_{3/2}$ at 350.5 and 347 eV, respectively, ensuring a +2 oxidation state of Ca. The deconvoluted Mn 2p spectrum in Fig. 1(f) consists of two prominent peaks at 641.7 and 653 eV corresponding to Mn $2p_{3/2}$ and Mn $2p_{1/2}$ states, respectively. This shows the oxidation state of Mn lies between +3 and +4 [38,39], confirming the $CaMnO_{3-\delta}$ phase in CMO. The top view FESEM image of the CMO thin film (Fig. S1 in the Supplemental Material [40]) shows a granular film with voids.

Optical absorption spectra of CMO thin films were measured in the wavelength range of 800–350 nm, as shown in Fig. 2(a). The absorption edge starts at the wavelength of ∼750 nm, and the absorption coefficient increases to a value $> 10^4$ cm^{-1} at the wavelength of ∼700 nm, reaching a maximum value $> 6 \times 10^4$ cm^{-1} at ∼400 nm. The inset of the absorption spectra shows the optical image of the CMO film on a glass substrate, and the dark brown color agrees with their absorption spectra. The Tauc plot in Fig. 2(b) shows two prominent direct optical bandgaps at 1.77 eV (E_{g1}) and 2.25 eV (E_{g2}). The E_{g1} value is like the value reported for the pulsed-laser-deposited $CaMnO_3$ films [33]. To further clarify our optical data and their correlation with the band structure,

TABLE I. Allowed optical transitions and their corresponding optical energy levels.

Allowed transitions	$\Gamma_1 \rightarrow \Gamma_5$	$\Gamma_1 \rightarrow \Gamma_6$	$\Gamma_1 \rightarrow \Gamma_7$	$\Gamma_1 \rightarrow \Gamma_8$
Energy gap (eV)	1.47	1.55	1.64	2.46

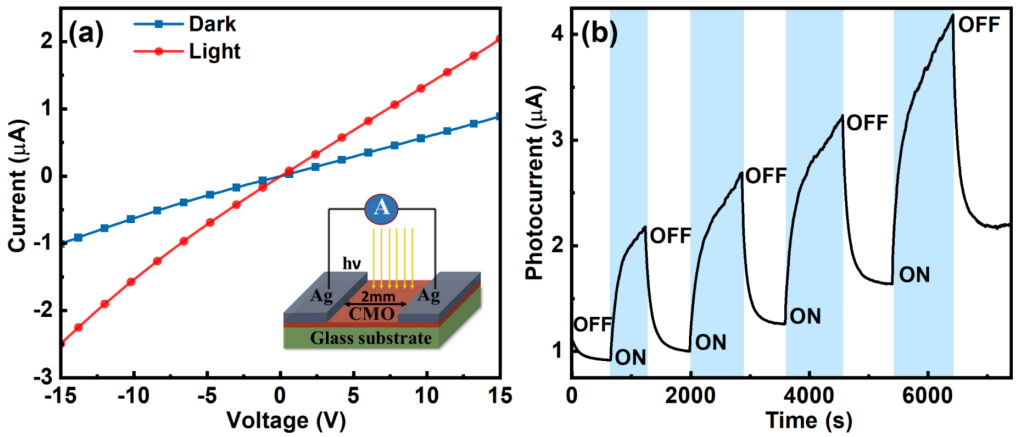

FIG. 3. (a) The current-voltage curves of pure CMO film in dark and under illumination (for 5 min). Inset shows the three-dimensional schematic of the photoresponse measurement setup. (b) The photocurrent time response of CMO films at 15 V as a function of illumination.

we performed first-principles calculations of CMO within the DFT framework implemented in QUANTUM ESPRESSO [41] and following previous reports [42]. The details of the calculation methodology are given in Supplemental Material Note S1 [40]. The electronic band structure and the density of states (DOS) are shown in Figs. 2(c) and 2(d), respectively. To better understand the transition levels, some points at the zone center (from Γ1 to Γ8) in the *E*-*K* diagram have been marked in Fig. 2(c). The band structure shows an electronic transition with a direct bandgap of 1.32 eV between the upper and lower Mott-Hubbard bands (Γ4 → Γ5). The valence band maxima have overwhelmingly O 2*p* character. However, there is also a tiny contribution from the Mn 3*d* orbitals, resulting in a hybridized state between these two sets of orbitals. In contrast to the valence band maxima, the Mn 3*d* orbital has the largest contribution to the conduction band minima, while the contribution of O 2*p* is almost equal to that of the Mn 3*d* orbital. The estimated bandgap value is closer to the value reported earlier [43]. However, CMO has a *Pnma* space group with inversion symmetry; hence, the electric-dipole operator with odd parity can enable optical transitions between states with opposite parities only [28,44]. A detailed discussion of the allowed transitions is given in Supplemental Material Note S2 [40]. Since valence band states Γ2, Γ3, and Γ4 have the same even parity with the conduction band states from Γ5 to Γ8 (corresponding to the Mn 3*d* bands), transitions between these levels are forbidden. The allowed transitions are from the Γ1 position of the valence band (corresponding to O 2*p*) to the Mn 3*d* bands in the conduction band. The estimated transition values are given in Table I, and these values closely match the absorption data. The room temperature PL spectrum [Fig. 2(e)] of the CMO films shows a strong emission peak ∼3.18 eV and a broad emission at 1.72 eV, consistent with the absorption data. The existence of emission confirms the direct bandgap nature of CMO as obtained from DFT calculations and the Tauc plot.

To study the photoresponse of the solution-grown CMO thin film, current vs voltage characteristics under dark and light (from a xenon light source) were measured, and the plot is depicted in Fig. 3(a). Linear *I*-*V* characteristics both under the dark and illumination confirm the ohmic contact of silver with CMO. A 2.5 times increase in the photocurrent values over the dark current at a bias of 15 V in Fig. 3(a) and a steady rise under illumination in the transient photocurrent response in Fig. 3(b) confirm that the CMO films are sensitive to light.

The suitable optical and photoconducting properties of solution-grown thin films prompted us to study the photovoltaic properties of CMO. Conventional sensitized solar cells in an all oxide combination were prepared, and the typical

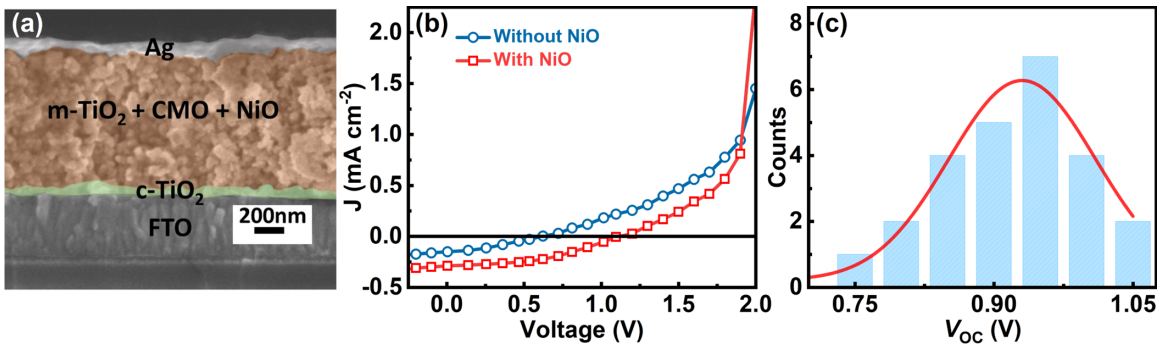

FIG. 4. (a) Cross-section field emission scanning electron microscope (FESEM) image of the solar cell. (b) *J*-*V* characteristics of solar cell with and without NiO hole transporting layer (HTL) under 1 sun illumination. (c) Histogram of the V_{OC} of 25 conventional solar cells with NiO HTL.

TABLE II. Solar cell device parameters of devices with and without NiO HTL layer.

Device architecture	V_{OC} (V)	I_{SC} (mA cm^{-2})	Fill factor (%)	Efficiency (%)
Without NiO	0.53 ± 0.12	0.150 ± 0.033	32 ± 3	0.03 ± 0.01
With NiO	0.92 ± 0.17	0.292 ± 0.022	43 ± 2	0.12 ± 0.04

structure of fabricated solar cells is given in the cross-sectional FESEM image in Figs. 4(a) and S2 in the Supplemental Material [40]. The phase formation of the CMO deposited on m-TiO_2 was also verified using XRD and XPS, as plotted in Fig. S3 in the Supplemental Material [40]. We also prepared solar cells without the NiO layer to study the charge separation capability of CMO. Current density vs voltage (J-V) characteristics were measured using a Keithley 2450 source meter under 1 sun illumination from a AAA solar simulator (Abet 11000A). Figure 4(b) shows the current density vs voltage (J-V) characteristics of the best-performing devices for both types of solar cells. A simple mesostructured heterojunction composed of wide bandgap TiO_2 ETL coated with CMO absorber offers the V_{OC} of ~0.6 V, which is missing in the m-TiO_2/NiO heterojunction (Fig. S4(a) in the Supplemental Material [40]), confirming the photovoltaic effect in the CMO absorber. The addition of the NiO HTL increases the V_{OC} to a value of the order of 1 V. To check the reliability of the devices, 25 solar cells of each type were fabricated, and the cell parameters are listed in Table II. The average V_{OC} for the devices without NiO was 0.53 V, with a maximum of 0.6 V (Fig. S4(b) in the Supplemental Material [40]), whereas an average V_{OC} of 0.92 V [Fig. 4(c)] with a maximum of 1.03 V was achieved in the conventional structure. The average V_{OC} obtained here is among the highest for metal-oxide-absorber-based solar cells reported so far [45], as given in Table S1 in the Supplemental Material [40].

Proper band alignment of the active absorber layer with the ETL and HTL plays a crucial role in efficient charge collection and achieving high V_{OC} in sensitized solar cells [46,47]. To determine the band alignment of the active absorber layer, we have combined UPS with the UV-visible absorption spectra [48]. Figure 5(a) shows the UPS spectra of the CMO layer on m-TiO_2, and the estimated ionization energy from the width of the spectra is −5.29 eV. Considering the experimental optical bandgap of 1.77 eV, the calculated electron affinity is −3.52 eV. The schematic of the energy band configuration of the CMO with the TiO_2 ETL and NiO HTL is given in Fig. 5(b), and the conduction band positions of the ETL and the valence band position of the HTL are taken from the previous reports [49,50]. We simulated our solar cells using SCAPS software to estimate the origin of higher voltage

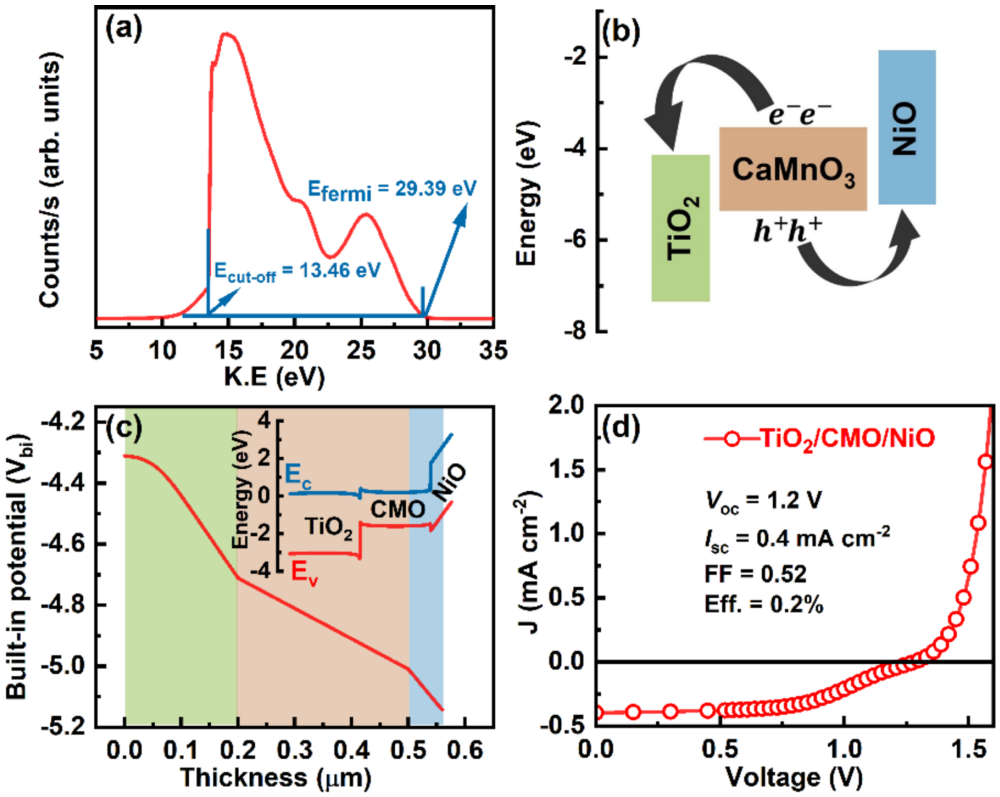

FIG. 5. (a) Ultraviolet photoelectron spectroscopy (UPS) of CMO [work function (Φ) = 21.22 eV (photon energy) − (29.39–13.46 eV)]. (b) Schematic energy level diagram of the heterojunction. (c) Simulated built-in potential (V_{bi}) variation across the interfaces, and inset shows the simulated energy band offsets of c-TiO_2/m-TiO_2/CMO/NiO heterojunction. (d) Simulated J-V curve of CMO-based conventional solar cell.

using the same band alignment. The optical and electrical parameters used in the theoretical calculations are taken from Ref. [51] and are listed in Table S2 in the Supplemental Material [40]. The distribution of the simulated built-in potential within the mesostructured TiO_2/CMO/NiO heterojunction in Fig. 5(c) shows a gradual decrease in the potential that plays a vital role in the charge separation in the sensitized solar cells. The higher V_{OC} is likely attributed to the higher built-in potential within the heterojunction due to the large band offsets of the absorber layer with the transporting layers [52,53], as given in the inset of Fig. 5(c). The simulated J-V curve of the proposed heterojunction in Fig. 5(d) also shows a V_{OC} value of 1.2 eV, in agreement with the experimental observation.

Although we have achieved a high V_{OC}, the champion CMO-based conventional solar cell shows a power conversion efficiency of ∼0.1%, with an average efficiency of 0.08% (Table II). The spin coating of CMO leads to incomplete surface coverage and insufficient pore filling of the absorber layer within the m-TiO_2 scaffold, which is evident from the nonuniform porous structure of the m-TiO_2 + CMO layer, as shown in the top view FESEM image in Fig. S5(a) in the Supplemental Material [40]. This, in turn, reduces the overall absorption capacity of the CMO layer (optical images in Figs. S5(b) and 5(c) in the Supplemental Material [40]), limiting the value of J_{SC}. Furthermore, we performed the EDX spectra analysis along the cross-section of the solar cell to determine the distribution of elements within the layers. The homogeneous distribution of Ti, Ca, Mn, and Ni, within the m-TiO_2 + CMO + NiO in Fig. S6 in the Supplemental Material [40] confirms the lower pore filling of m-TiO_2 by CMO, which will lead to lower shunt resistance for the TiO_2/CMO/NiO heterostructure, resulting in lower fill factor (FF) [54]. Electrochemical impedance spectroscopy was employed to understand the factors responsible for the low short-circuit current density (J_{SC}) and FF in CMO-based all oxide solar cells. The impedance spectrum was recorded at 500 mV amplitude over the frequency range of 1 Hz to 1 MHz using an electrochemical workstation (CHI 1150C, CH Instruments), and the corresponding fitted Nyquist plot is shown in Fig. S7 in the Supplemental Material [40]. The electronic parameters such as series resistance (R_s), charge transfer resistance (R_{CT}), recombination resistance (R_{rec}), and constant phase elements (C_1, C_2) were simulated using ZSIM software and are given in Table S3 in the Supplemental Material [40]. A high charge transfer resistance of ∼93 kΩ and a low recombination resistance of 2.3 kΩ are likely to reduce the J_{SC} and FF [55], respectively, for the solution-processed CMO-based all oxide solar cells.

IV. CONCLUSIONS

In summary, we systematically explored the optical and photovoltaic properties of CMO thin films synthesized by the simple solution-processed spin coating method. Optical studies revealed that solution-processed CMO has a direct optical bandgap at ∼1.77 eV with an absorption coefficient as high as 10^4 cm^{-1}. The first-principles calculations show that electronic transitions between O 2p and Mn 3d bands contribute to the optical absorption in the visible region. Photovoltaic properties of a CMO-based solar cell were investigated. Suitable band alignment with a large band offset of CMO with both the NiO HTL and TiO_2 ETL enables us to achieve an average V_{OC} of 0.92 V with a maximum of 1.03 V, which was further validated using simulations. Our results suggest that CMO can be used as a low-cost alternative solar absorber material. Low pore filling of m-TiO_2 by the active layer reduces overall light absorption, leading to low J_{SC}, and a low recombination resistance lowers the FF, limiting the overall photoconversion efficiency. Further optimization is required in terms of CMO film quality, use of different ETLs and HTLs, and suitable device architecture to significantly improve the efficacy of the CMO-based solar cells and use the same in tandem solar cell design.

ACKNOWLEDGMENT

We acknowledge the Science and Engineering Research Board, Government of India, via Project No. SRG/2019/000602.

[1] S. Okamoto, J. Nichols, C. Sohn, S. Y. Kim, T. W. Noh, and H. N. Lee, Nano Lett. **17**, 2126 (2017).
[2] S. Roy and N. Ali, J. Appl. Phys. **89**, 7425 (2001).
[3] R. Mahendiran, A. Maignan, S. Hébert, C. Martin, M. Hervieu, B. Raveau, J. F. Mitchell, and P. Schiffer, Phys. Rev. Lett. **89**, 286602 (2002).
[4] H. Oshima, K. Miyano, Y. Konishi, M. Kawasaki, and Y. Tokura, Appl. Phys. Lett. **75**, 1473 (1999).
[5] S. P. Jiang, J. Mater. Sci. **43**, 6799 (2008).
[6] A. Xukeer, Z. Wu, Q. Sun, F. Zhong, M. Zhang, M. Long, and H. Duan, RSC Adv. **10**, 30428 (2020).
[7] C. M. Widdifield, I. Moudrakovski, and D. L. Bryce, Phys. Chem. Chem. Phys. **16**, 13340 (2014).
[8] X. Gao, G. Liu, Y. Zhu, P. Kreider, A. Bayon, T. Gengenbach, T. Lu, Y. Liu, J. Hinkley, W. Lipiński *et al.*, Nano Energy **50**, 347 (2018).
[9] E. Ekström, A. le Febvrier, D. Fournier, J. Lu, V.-L. Ene, N. Van Nong, F. Eriksson, P. Eklund, and B. Paul, J. Mater. Sci. **54**, 8482 (2019).
[10] X. Han, Y. Hu, J. Yang, F. Cheng, and J. Chen, Chem. Commun. **50**, 1497 (2014).
[11] E. Mastronardo, X. Qian, J. M. Coronado, and S. M. Haile, J. Energy Storage **40**, 102793 (2021).
[12] J. Du, T. Zhang, F. Cheng, W. Chu, Z. Wu, and J. Chen, Inorg. Chem. **53**, 9106 (2014).
[13] K. Pandey, D. Singh, S. K. Gupta, P. Yadav, Y. Sonvane, I. Lukačević, M. Kumar, M. Kumar, and R. Ahuja, Nano Energy **45**, 287 (2018).
[14] A. Bera, A. D. Sheikh, M. A. Haque, R. Bose, E. Alarousu, O. F. Mohammed, and T. Wu, ACS Appl. Mater. Interfaces **7**, 28404 (2015).

[15] S. S. Shin, S. J. Lee, and S. I. Seok, APL Mater. **7**, 022401 (2019).

[16] A. Bera, K. Wu, A. Sheikh, E. Alarousu, O. F. Mohammed, and T. Wu, J. Phys. Chem. C **118**, 28494 (2014).

[17] J. Jung, D. L. Kim, S. H. Oh, and H. J. Kim, Sol. Energy Mater. Sol. Cells **102**, 103 (2012).

[18] C. Tao, S. Ruan, G. Xie, X. Kong, L. Shen, F. Meng, C. Liu, X. Zhang, W. Dong, and W. Chen, Appl. Phys. Lett. **94**, 043311 (2009).

[19] V. Shrotriya, G. Li, Y. Yao, C.-W. Chu, and Y. Yang, Appl. Phys. Lett. **88**, 073508 (2006).

[20] B. Kupfer, K. Majhi, D. A. Keller, Y. Bouhadana, S. Rühle, H. N. Barad, A. Y. Anderson, and A. Zaban, Adv. Energy Mater. **5**, 1401007 (2015).

[21] S. Shibasaki, Y. Honishi, N. Nakagawa, M. Yamazaki, Y. Mizuno, Y. Nishida, K. Sugimoto, and K. Yamamoto, Appl. Phys. Lett. **119**, 242102 (2021).

[22] T.-Y. Cai, S.-C. Liu, S. Ju, C.-Y. Liu, and G.-Y. Guo, Phys. Rev. Appl. **8**, 034034 (2017).

[23] W. S. Choi, M. F. Chisholm, D. J. Singh, T. Choi, G. E. Jellison, and H. N. Lee, Nat. Commun. **3**, 689 (2012).

[24] R. Nechache, C. Harnagea, S. Li, L. Cardenas, W. Huang, J. Chakrabartty, and F. Rosei, Nat. Photonics **9**, 61 (2015).

[25] A. Zenkevich, Y. Matveyev, K. Maksimova, R. Gaynutdinov, A. Tolstikhina, and V. Fridkin, Phys. Rev. B **90**, 161409(R) (2014).

[26] W. Ji, K. Yao, and Y. C. Liang, Phys. Rev. B **84**, 094115 (2011).

[27] D. Tiwari, D. J. Fermin, T. K. Chaudhuri, and A. Ray, J. Phys. Chem. C **119**, 5872 (2015).

[28] L. Wang, Y. Li, A. Bera, C. Ma, F. Jin, K. Yuan, W. Yin, A. David, W. Chen, W. Wu *et al.*, Phys. Rev. Applied **3**, 064015 (2015).

[29] I. Grinberg, D. V. West, M. Torres, G. Gou, D. M. Stein, L. Wu, G. Chen, E. M. Gallo, A. R. Akbashev, P. K. Davies *et al.*, Nature (London) **503**, 509 (2013).

[30] F. Wang, I. Grinberg, and A. M. Rappe, Phys. Rev. B **89**, 235105 (2014).

[31] Y. H. Paik, H. S. Kojori, J.-H. Yun, and S. J. Kim, Mater. Lett. **185**, 247 (2016).

[32] N. N. Loshkareva, L. V. Nomerovannaya, E. V. Mostovshchikova, A. A. Makhnev, Y. P. Sukhorukov, N. I. Solin, T. I. Arbuzova, S. V. Naumov, N. V. Kostromitina, A. M. Balbashov *et al.*, Phys. Rev. B **70**, 224406 (2004).

[33] P. Zhao, J. Xu, H. Wang, L. Wang, W. Kong, W. Ren, L. Bian, and A. Chang, J. Appl. Phys. **116**, 194901 (2014).

[34] E. Suprayoga, W. B. K. Putri, K. Singsoog, S. Paengson, M. Y. Hanna, A. R. T. Nugraha, D. R. Munazat, B. Kurniawan, M. Nurhuda, T. Seetawan *et al.*, Mater. Res. Bull. **141**, 111359 (2021).

[35] A. Göktaş, A. Tumbul, and F. Aslan, J. Sol-Gel Sci. Technol. **78**, 262 (2016).

[36] K. R. Nandan and A. R. Kumar, J. Mater. Res. Technol. **8**, 2996 (2019).

[37] O. A. G. Wahba, A. M. Hassan, H. A. El-wahab, A. Mohy-Eldin, A. M. Naser, and O. A. Fouad, Pigment Resin Technol. **44**, 379 (2015).

[38] S. Kumar, V. S. Raju, S. Bera, K. Vijaynandhini, and T. R. N. Kutty, Nuc. Inst. Met. Phys. Res. B **237**, 623 (2005).

[39] X. Han, T. Zhang, J. Du, F. Cheng, and J. Chen, Chem. Sci. **4**, 368 (2013).

[40] See Supplemental Material at http://link.aps.org/supplemental/10.1103/PhysRevMaterials.6.085402 for FESEM Images, DFT calculation details, detailed discussion on allowed transitions in the band structure, XRD and XPS spectra of CMO on m-TiO2, J-V characteristics of mesostructured TiO_2/NiO heterojunction, histogram of VOC for solar cells without HTL, VOC comparison of our device with other oxide-absorber-based solar cells, details of the simulation, cross-sectional EDX images, Nyquist plot, and the fitted parameters.

[41] P. Giannozzi, S. Baroni, N. Bonini, M. Calandra, R. Car, C. Cavazzoni, D. Ceresoli, G. L. Chiarotti, M. Cococcioni, I. Dabo *et al.*, J. Phys. Condens. Matter **21**, 395502 (2009).

[42] Computational methodology and the detailed discussion of the allowed transitions is given in Note S2 in the Supplemental Material [40] which includes Refs. [41,56–62].

[43] A. Shinde, S. K. Suram, Q. Yan, L. Zhou, A. K. Singh, J. Yu, K. A. Persson, J. B. Neaton, and J. M. Gregoire, ACS Energy Lett. **2**, 2307 (2017).

[44] A. Walsh, J. L. F. Da Silva, S.-H. Wei, C. Körber, A. Klein, L. F. J. Piper, A. DeMasi, K. E. Smith, G. Panaccione, P. Torelli *et al.*, Phys. Rev. Lett. **100**, 167402 (2008).

[45] The comparison of V_{OC} for metal oxide absorber-layer-based solar cells was done with Refs. [25,27,28,31,63–70].

[46] J. Robertson, J. Vac. Sci. Technol. B **18**, 1785 (2000).

[47] A. Klein, Thin. Solid. Films **520**, 3721 (2012).

[48] J. W. Kim and A. Kim, Curr. Appl. Phys. **31**, 52 (2021).

[49] S. S. Shin, S. J. Lee, and S. Il Seok, Adv. Funct. Mater. **29**, 1900455 (2019).

[50] H. H. Park, Nanomaterials **12**, 112 (2021).

[51] The details of the device simulation through SCAPS and the optical and electrical parameters used in the theoretical calculations are listed in Table S2 in the Supplemental Material [40] comprising Refs. [32,34,71–73].

[52] S. Ahmmed, A. Aktar, J. Hossain, and A. B. M. Ismail, Sol. Energy **207**, 693 (2020).

[53] O. J. Sandberg, J. Kurpiers, M. Stolterfoht, D. Neher, P. Meredith, S. Shoaee, and A. Armin, Adv. Mater. Interfaces **7**, 2000041 (2020).

[54] I.-K. Ding, N. Tétreault, J. Brillet, B. E. Hardin, E. H. Smith, S. J. Rosenthal, F. Sauvage, M. Grätzel, and M. D. McGehee, Adv. Funct. Mater. **19**, 2431 (2009).

[55] P. P. Boix, G. Larramona, A. Jacob, B. Delatouche, I. Mora-Seró, and J. Bisquert, J. Phys. Chem. C **116**, 1579 (2012).

[56] P. E. Blöchl, Phys. Rev. B **50**, 17953 (1994).

[57] A. Dal Corso, A. Pasquarello, A. Baldereschi, and R. Car, Phys. Rev. B **53**, 1180 (1996).

[58] J. P. Perdew, K. Burke, and M. Ernzerhof, Phys. Rev. Lett. **77**, 3865 (1996).

[59] J. P. Perdew, A. Ruzsinszky, G. I. Csonka, O. A. Vydrov, G. E. Scuseria, L. A. Constantin, X. L. Zhou, and K. Burke, Phys. Rev. Lett. **100**, 136406 (2008).

[60] V. I. Anisimov, J. Zaanen, and O. K. Andersen, Phys. Rev. B **44**, 943 (1991).

[61] J. H. Jung, K. H. Kim, D. J. Eom, T. W. Noh, E. J. Choi, J. Yu, Y. S. Kwon, and Y. Chung, Phys. Rev. B **55**, 15489 (1997).

[62] U. Aschauer, R. Pfenninger, S. M. Selbach, T. Grande, and N. A. Spaldin, Phys. Rev. B **88**, 054111 (2013).

[63] S. Chatterjee, S. K. Saha, and A. J. Pal, Sol. Energy Mater. Sol. Cells **147**, 17 (2016).

[64] A. Kaphle, E. Echeverria, D. N. Mcllroy, and P. Hari, RSC Adv. **10**, 7839 (2020).

[65] Z. Fan, K. Yao, and J. Wang, Appl. Phys. Lett. **105**, 162903 (2014).

[66] S. Chatterjee, A. Bera, and A. J. Pal, ACS Appl. Mater. Interfaces **6**, 20479 (2014).

[67] K. Majhi, L. Bertoluzzi, K. J. Rietwyk, A. Ginsburg, D. A. Keller, P. Lopez-Varo, A. Y. Anderson, J. Bisquert, and A. Zaban, Adv. Mater. Interfaces **3**, 1500405 (2016).

[68] M. Sariful Sheikh, D. Ghosh, A. Dutta, S. Bhattacharyya, and T. P. Sinha, Mater. Sci. Eng. B **226**, 10 (2017).

[69] Y. G. Zhang, H. W. Zheng, J. X. Zhang, G. L. Yuan, W. X. Gao, Y. Z. Gu, C. L. Diao, Y. F. Liu, and W. F. Zhang, Mater. Lett. **125**, 25 (2014).

[70] S. Kooriyattil, R. K. Katiyar, S. P. Pavunny, G. Morell, and R. S. Katiyar, Appl. Phys. Lett. **105**, 072908 (2014).

[71] S. Sarkar, V. Gupta, M. Kumar, J. Schubert, P. T. Probst, J. Joseph, and T. A. F. König, ACS Appl. Mater. Interfaces **11**, 13752 (2019).

[72] T. C. Peng, X. H. Xiao, X. Y. Han, X. D. Zhou, W. Wu, F. Ren, and C. Z. Jiang, Appl. Surf. Sci. **257**, 5908 (2011).

[73] K. Deepthi Jayan and V. Sebastian, Sol. Energy **217**, 40 (2021).